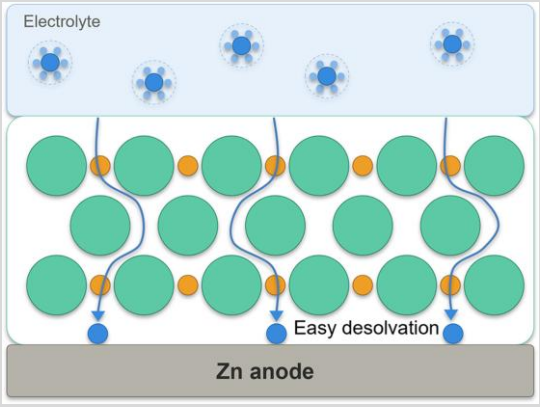
Research Article

Zinc Pre-embedded Carbon Dots Enabling Highly Reversible Zinc Metal Anodes for Aqueous Zinc-ion Batteries

SUN Haowen, HE Tianle, ZHANG Xirong, XIAO Ling and XIONG Huanming✉

Received August 28, 2026
Accepted October 9, 2026
© Jilin University, The Editorial Department of Chemical Research in Chinese Universities and Springer-Verlag GmbH

Aqueous zinc-ion batteries (AZIBs) hold great promise for large-scale energy storage, yet their practical application is hindered by dendrite growth, corrosion, and hydrogen evolution at the Zn anode. Carbon dots (CDs) are attractive coating materials for anode protection owing to their abundant zincophilic functional groups; however, their spontaneous aggregation into densely packed layers buries these groups and blocks ion-transport pathways, compromising their regulatory function. Herein, we resolve this dilemma *via* a zinc pre-embedding strategy: zinc pre-embedded carbon dots (zCD), synthesized through an ethanol-assisted solvothermal route, are coated onto Zn foil as a hydrophobic yet zincophilic protective layer (zCD@Zn). The pre-embedded Zn^{2+} acts as inter-particle spacers that suppress dense CD stacking, preserving continuous ion-transport channels while keeping the zincophilic groups accessible. The zCD layer thus shields the anode from water-induced parasitic reactions, reconstructs the Zn^{2+} solvation sheath (desolvation energy of 16.31 kJ/mol), and elevates the Zn^{2+} transference number to 0.79, collectively enabling uniform, dendrite-free Zn deposition. As a result, the zCD@Zn symmetric cell operates stably for over 1000 h at 1 mA/cm² and 1 mA·h·cm⁻², and Zn||Cu half cells deliver an average Coulombic efficiency of 99.5% over 800 cycles. Paired with an MnO_2 cathode, the full cell retains 87.9% of its capacity after 800 cycles at 1 A/g and 90.7% after a 48 h rest. This work establishes metal-ion pre-embedding as a generalizable strategy to unlock the interfacial potential of aggregation-prone nanomaterials for highly reversible metal anodes.



Keywords Aqueous zinc-ion battery; Zinc metal anode; Carbon dot; Zinc pre-embedding; Interfacial engineering

1 Introduction

Aqueous zinc-ion batteries (AZIBs) have emerged as a prominent research topic in recent years due to their inherent safety compared to commercial lithium-ion batteries (LIBs) that employ flammable organic electrolytes, along with advantages including the high ionic conductivity of aqueous electrolytes, straightforward fabrication processes, and environmental friendliness.[1,2] Zinc metal possesses unique strengths as the anode material for AZIBs, such as low production costs resulting from the high natural abundance of zinc and mature processing technologies, enabling large-scale industrial manufacturing.[3] Moreover, the theoretical capacity of the zinc anode is high (820 mA·h·g⁻¹ and 5855 mA·h·cm⁻³), as the two-electron redox chemistry of Zn^{2+}/Zn endows AZIBs with a high theoretical volumetric energy density, making them promising candidates for large-scale stationary energy storage.[4] However, the zinc anode faces multiple challenges, including dendrite growth, corrosion, and hydrogen evolution reaction (HER), which severely degrade the cycle life of AZIBs in practical applications. These critical limitations necessitate the development of innovative technical solutions.[5]

In the past few years, various effective strategies have been proposed to address these challenges and enhance the cyclic stability of AZIBs, including constructing a protective coating layer on the zinc anode surface, optimizing electrolyte formulations, and employing functionalized separators.[6,7] Among these approaches, the direct fabrication of a protective coating layer on the zinc anode surface stands out owing to its facile fabrication and high practical applicability.[8] A wide variety of materials have been developed as protective coating layers for zinc anodes, including carbon-based materials,[9] metals and alloys,[10,11] metal oxides,[12] sulfides,[13] MOF-derived materials,[14]

✉ XIONG Huanming
hmxiong@fudan.edu.cn
Department of Chemistry, Shanghai Key Laboratory of Electrochemical and Thermochemical Conversion for Resources Recycling, Fudan University, Shanghai 200438, P. R. China

https://doi.org/10.1007/s40242-026-6206-x

inorganic salts,[15] polymeric materials,[16] and organic-inorganic hybrid materials.[17] Among these materials, some coating layers exhibit hydrophobic properties that can prevent direct contact between the zinc anode and free water molecules in the electrolyte, thereby suppressing side reactions.[18] In addition, some protective layers can provide abundant zincophilic nucleation sites, which induce uniform zinc deposition and inhibit dendrite growth.[19] Consequently, the development of a protective coating layer that integrates these dual functions has emerged as a key research focus.[20]

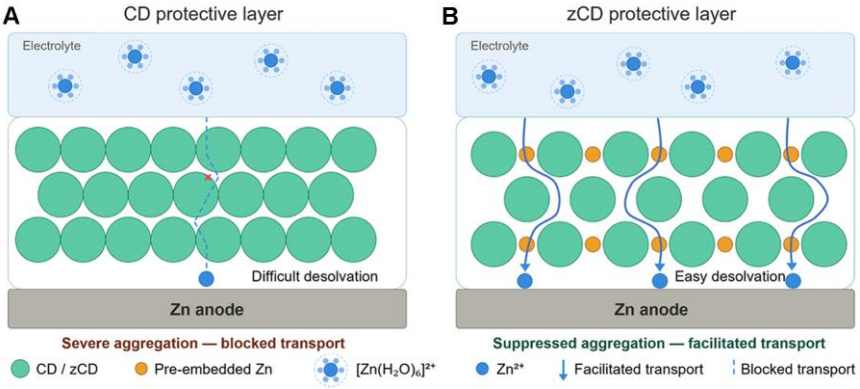
Carbon dots (CDs), an emerging class of zero-dimensional nanomaterials with sizes typically below 10 nm, have attracted considerable attention for applications in biomedicine, catalysis, and energy storage owing to their abundant and tunable functional groups, excellent dispersibility, good biocompatibility, and diverse precursor sources.[21,22] Recent studies have demonstrated that the functional groups on CDs can significantly increase the density of Zn^{2+} nucleation sites, lower the Zn^{2+} nucleation barrier, and suppress the two-dimensional (2D) diffusion of Zn^{2+} on the anode surface, thereby enabling homogeneous zinc deposition in AZIBs.[23,24] In our previous work, nitrogen-doped carbon dots (NCDs) were designed and applied to control the growth of mesoporous TiO_2. The TiO_2/NCDs composite was coated on the zinc foil surface as a protective layer. The results demonstrated that TiO_2/NCDs could effectively inhibit dendrite growth and corrosion, and induce the electrodeposited Zn to grow into a stable petal-like morphology. The Zn-TiO_2/NCDs anode exhibited a prolonged cycling lifespan, demonstrating the considerable promise of CDs for enhancing the reversibility of the zinc anode.[25]

In this work, zinc pre-embedded carbon dots (zCD) exhibiting both hydrophobic and zincophilic properties were synthesized *via* an ethanol-assisted solvothermal method and directly coated onto the zinc anode surface as a protective layer to enhance cycling stability. On one hand, the hydrophobic nature of the zCD protective layer prevents direct contact between the zinc anode and the aqueous electrolyte, thereby suppressing corrosion and hydrogen evolution reaction (HER). On the other hand, the zincophilic functional groups (carbonyl, hydroxyl, and amino groups) on the zCD surface reconstruct the Zn^{2+} solvation sheath through dynamic coordination, guiding uniform Zn^{2+} deposition. Furthermore, the zinc pre-embedding strategy mitigates the dense packing of CDs and renders the zincophilic functional groups more accessible, effectively improving the Zn^{2+} transport kinetics. The symmetric cell assembled with zCD@Zn exhibited a long cycling lifespan of 1000 h at 1.0 mA/cm² and 1.0 mA·h·cm^{-2}. Moreover, when paired with an MnO_2 cathode, the zCD@Zn-based full cell retained 87.9% of its reversible capacity after 800 cycles.

2 Results and Discussion

Owing to their nanoscale dimensions and high surface energy, CDs tend to aggregate when employed as a protective coating, giving rise to dense particle stacking. This aggregation exerts two adverse effects: (i) the majority of zincophilic functional groups are buried within the aggregates and become inaccessible, weakening their capability to regulate Zn^{2+} desolvation and homogeneous nucleation; (ii) the inter-particle voids are largely eliminated, which impedes Zn^{2+} transport across the coating. To address these issues, we pre-embedded Zn^{2+} into CDs by coordinating Zn^{2+} with the surface functional groups during synthesis. The pre-embedded Zn^{2+} occupies the coordination sites of the functional groups, weakening the inter-CD interactions (*e.g.*, hydrogen bonding) that drive aggregation, while simultaneously introducing steric hindrance that prevents intimate contact between CDs. Consequently, dense stacking is suppressed and continuous inter-particle channels are preserved, with the zincophilic sites remaining accessible, which is expected to substantially enhance the Zn^{2+} transport kinetics within the protective layer (Scheme 1).

The morphology, optical properties, and composition of the as-prepared carbon dots were systematically investigated. High-resolution transmission electron microscopy (HRTEM) images (Fig. 1, A and B) reveal that both CD and zCD are nanoparticles with uniform diameters of approximately 3 nm, indicating that Zn^{2+} pre-embedding does not induce an appreciable change in the intrinsic particle size of the carbon dots. Moreover, the observed



Scheme 1 Schematic illustration of Zn plating behaviors on CD@Zn (A) and zCD@Zn (B) electrodes

https://doi.org/10.1007/s40242-026-6206-x

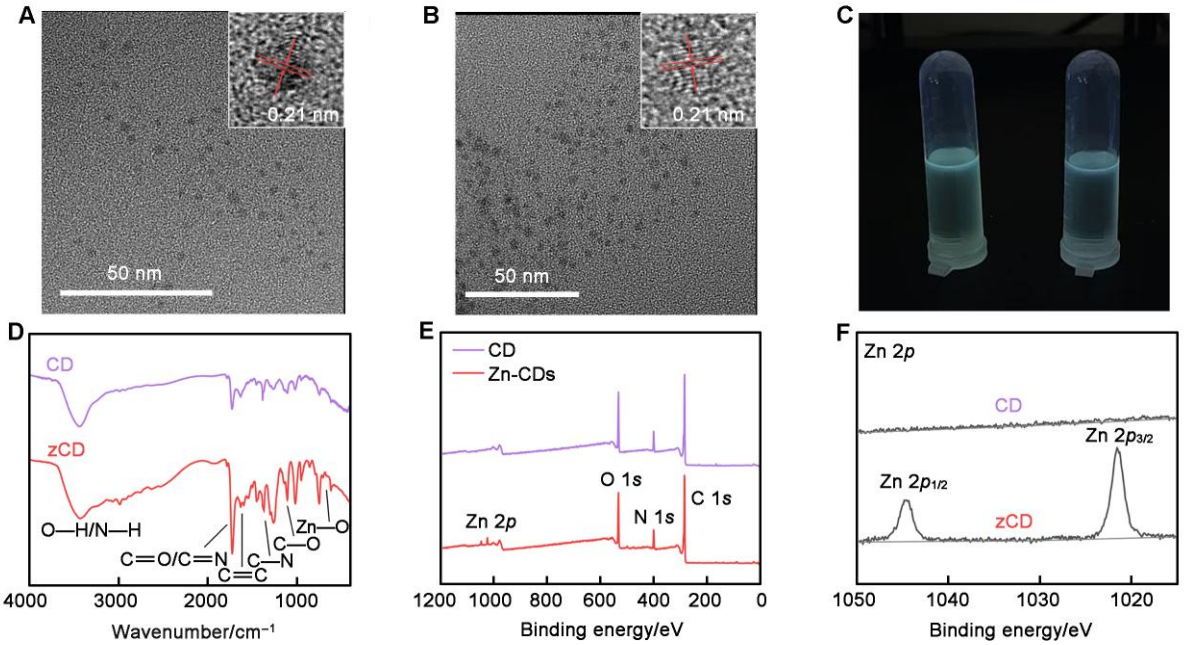


Fig. 1 Morphology, optical properties, and composition of the as-prepared carbon dots

(A, B) TEM and HRTEM (inset) images of CD (A) and zCD (B); (C) digital photographs of CD (left) and zCD (right) dispersed in DMSO under UV irradiation; (D, E) FTIR (D) and XPS (E) spectra of CD and zCD; (F) high-resolution Zn 2*p* XPS spectra.

in-plane lattice spacing of 0.21 nm corresponds to the (100) plane of graphite.[26] The low crystallinity of CD and zCD, characterized by short-range ordering, is further corroborated by X-ray diffraction (XRD) (Fig. S1B in the Supporting Information, SI), where both patterns exhibit a broad diffraction peak centered at 2θ *ca*. 22°, assignable to the (002) planes of the partially graphitized carbon core.[27] When dispersed in DMSO, both CD and zCD exhibit strong green fluorescence under UV irradiation (Fig. 1C), and their photoluminescence (PL) spectra (Fig. S1A in the SI) show a prominent emission peak at 530 nm under 410 nm excitation, confirming the characteristic photoluminescence property of carbon dots.[28]

The surface chemical composition was examined by Fourier transform infrared (FTIR) and X-ray photoelectron spectroscopy (XPS). In the FTIR spectra (Fig. 1D), the broad band at 3436 cm^{-1} is attributed to O—H/N—H stretching vibrations, while the bands at 1724, 1628, 1366, and 1104 cm^{-1} correspond to C=O/C=N, C=C, C—N, and C—O stretching, respectively.[29] Notably, a characteristic band at 455 cm^{-1}, assignable to Zn—O stretching, is exclusively observed in the zCD spectrum, providing direct evidence for the successful incorporation of zinc.[30] The XPS survey spectra (Fig. 1E) confirm the presence of C, N, and O in both samples; more importantly, Zn is detected only in zCD, as further verified by the high-resolution Zn 2*p* spectra (Fig. 1F), which together with the FTIR results, unambiguously demonstrate the successful pre-embedding of zinc into zCD. The high-resolution C 1*s* spectra of both CD and zCD (Fig. S2 in the SI) can be deconvoluted into C—C/C=C, C—O/C—N, and C=O components, while the N 1*s* spectra reveal the presence of pyridinic N, amino N, and pyrrolic N.[31] These results confirm that zCD retains the typical structural features of carbon dots while successfully incorporating pre-embedded zinc.

zCD was dispersed in an aqueous solution of sodium carboxymethyl cellulose (CMC-Na) to form a slurry, which was coated onto the Zn foil by blade coating to obtain the zCD@Zn electrode. The morphology of the coating layer was characterized by scanning electron microscopy (SEM). For the bare Zn foil, polishing scratches are visible on the surface (Fig. S3A in the SI); such microscopic unevenness is susceptible to localized corrosion by the electrolyte and induces tip effects that concentrate the local electric field, promoting Zn dendrite growth. In contrast, the zCD coating uniformly covers the Zn surface (Fig. 2A), preventing direct contact between the Zn foil and the electrolyte, and a similar protective layer is observed for CD@Zn (Fig. S3B in the SI). Under identical blade-coating conditions, cross-sectional SEM images of zCD@Zn (Fig. 2B) and CD@Zn (Fig. S3C in the SI) reveal comparable coating thicknesses of approximately 14 μm, thereby ensuring a consistent basis for the subsequent electrochemical comparison. The EDX elemental maps (Fig. S4 in the SI) show that C and O are homogeneously distributed on the Zn surface, confirming the even coverage of the zCD coating, which is expected to homogenize the electric field at the electrode/electrolyte interface and thereby facilitate uniform Zn deposition. Fig. S5 in the SI compares the XRD patterns of bare Zn, CD@Zn, and zCD@Zn. All three patterns exhibit the

https://doi.org/10.1007/s40242-026-6206-x

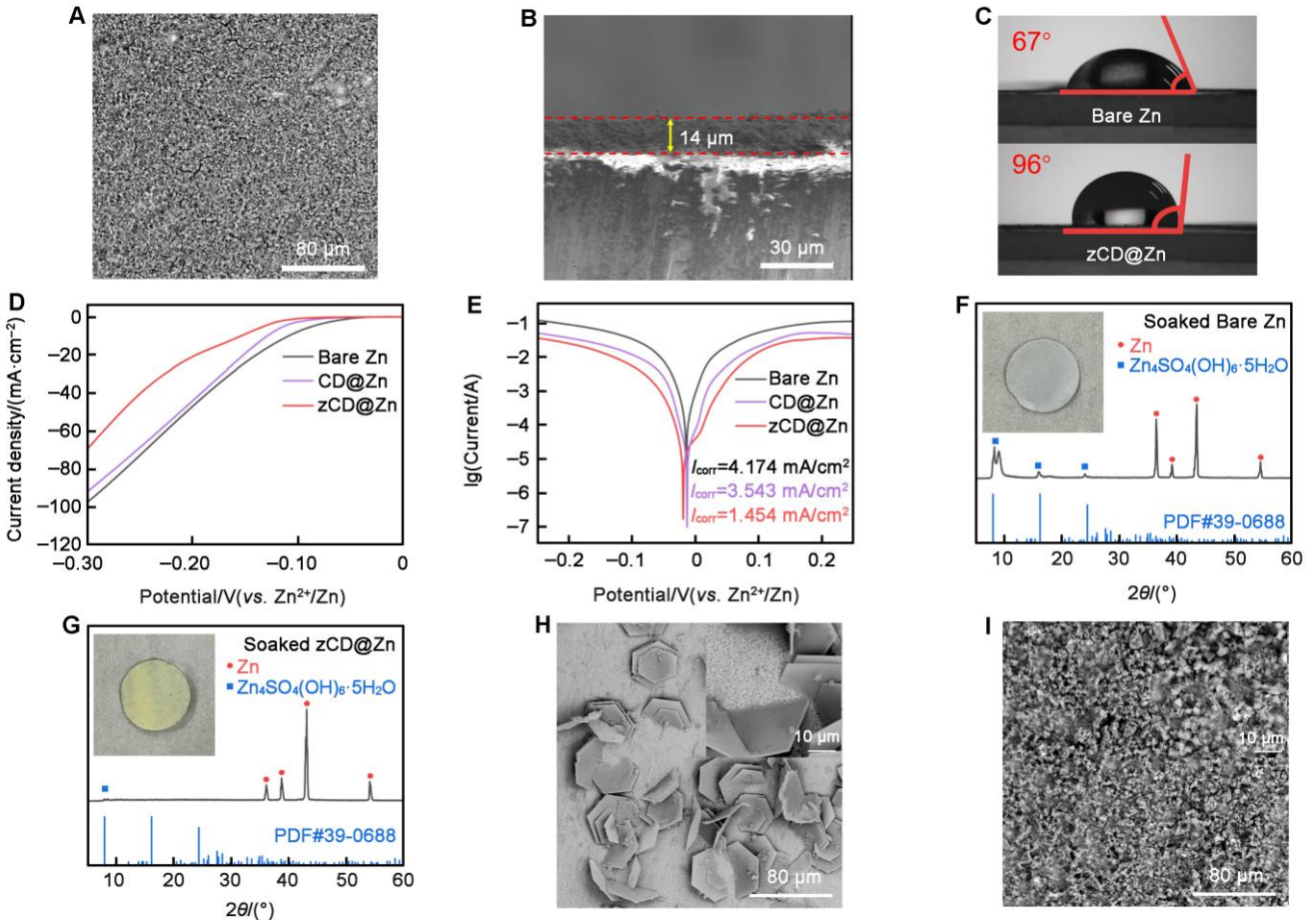


Fig. 2 Morphological characterization and corrosion-resistance validation of zCD@Zn

(A, B) Top-view (A) and cross-sectional (B) SEM images of zCD@Zn; (C) contact angles of the electrolyte on bare Zn (top) and zCD@Zn (bottom); (D, E) LSV curves (D) and Tafel polarization curves (E) of bare Zn, CD@Zn, and zCD@Zn; (F—I) XRD patterns of bare Zn (F) and zCD@Zn (G) (insets: digital photographs of the Zn foils in F and G), and SEM images of bare Zn (H) and zCD@Zn (I), after immersion in 2 mol/L $ZnSO_4$ for two weeks (insets: magnified views of the corresponding regions in H and I).

characteristic diffraction peaks of metallic Zn (PDF#04-0831). In addition, a broad peak centered at 2θ *ca.* 22°, characteristic of the carbon dot coatings, is observed only for CD@Zn and zCD@Zn, consistent with the XRD patterns of CD and zCD (Fig. S1B), confirming that the protective layer was successfully coated onto the Zn foil surface.

Water-induced corrosion and hydrogen evolution are recognized as the primary parasitic reactions that compromise the reversibility and cycling stability of Zn anodes in aqueous electrolytes; suppressing these side reactions is therefore essential for realizing highly reversible, long-life AZIBs.[32] The influence of the coating on the wettability of the Zn anode was evaluated by contact angle measurements (Fig. 2C and Fig. S6 in the SI). The contact angle between the bare Zn surface and the electrolyte is 67°, whereas those of CD@Zn and zCD@Zn are 94° and 96°, respectively. The increased contact angles indicate that both coatings exhibit enhanced hydrophobicity, which restricts the access of free water to the Zn surface and thus suppresses water-induced side reactions.[33] Benefiting from the hydrophobic character of the protective layers, both CD@Zn and zCD@Zn show substantially suppressed hydrogen evolution compared with bare Zn, as evidenced by the linear sweep voltammetry curves (LSV, Fig. 2D).[34] Tafel polarization measurements further corroborate the protective effect: zCD@Zn exhibits the lowest corrosion current density (1.454 mA/cm²) together with the most positive corrosion potential, outperforming CD@Zn and bare Zn (Fig. 2E).[35] To assess the long-term stability of the Zn anodes in the electrolyte, bare Zn, CD@Zn, and zCD@Zn were immersed in 2 mol/L $ZnSO_4$ electrolyte for two weeks. Well-defined hexagonal platelet-like by-products, identified by XRD as zinc hydroxide sulfate hydrate (ZHS, $Zn_4SO_4(OH)_6{\cdot}5H_2O$, PDF#39-0688), are clearly observed on the bare Zn surface after immersion (Fig. 2, F and H). By contrast, CD@Zn and zCD@Zn retain their original morphology without observable coating dissolution, and only negligible by-product peaks are detected (Fig. S7 in the SI and Fig. 2, G and I).[36] These results demonstrate that the hydrophobic zCD coating effectively and stably inhibits corrosion of the Zn anode in aqueous electrolytes.

Prior to the detailed interfacial kinetic analysis,

https://doi.org/10.1007/s40242-026-6206-x

electrochemical impedance spectroscopy (EIS) measurements on Zn||Zn symmetric cells were performed to evaluate the impact of the protective layers on ion transport. The results reveal that neither the CD nor the zCD coating introduces significant additional bulk resistance, confirming that they do not compromise the inherent high ionic conductivity of the aqueous electrolyte and thereby providing a reliable baseline for the subsequent kinetic investigations (Fig. S8 in the SI).

Beyond suppressing water-induced side reactions, the zCD coating is also expected to regulate Zn^{2+} transport and deposition kinetics at the electrode/electrolyte interface. To elucidate this, a series of electrochemical measurements was systematically performed. The activation energies (E_a) for Zn^{2+} desolvation were first derived from temperature-dependent EIS using the Arrhenius equation (Fig. 3A).[37] The zCD@Zn electrode exhibits the lowest E_a of 16.31 kJ/mol, substantially lower than that of bare Zn (24.80 kJ/mol), confirming that the exposed zincophilic functional groups on zCD effectively facilitate the desolvation of $[Zn(H_2O)_6]^{2+}$. Notably, CD@Zn shows an even higher E_a (30.83 kJ/mol) than bare Zn, indicating that the densely stacked CD coating not only fails to assist desolvation but imposes an additional energy barrier, as the majority of surface functional groups are buried within the aggregates and thus inaccessible to solvated Zn^{2+}. The Zn^{2+} transference numbers ($tz_{n^{2+}}$) were subsequently measured to assess ion transport selectivity (Fig. 3, B and C and Fig. S9 in the SI). Bare Zn exhibits a $tz_{n^{2+}}$ of 0.43, whereas CD@Zn shows a slightly lower value of 0.39, corroborating that the aggregated CD layer preferentially impedes Zn^{2+} migration over anion transport. In sharp contrast, zCD@Zn achieves a $tz_{n^{2+}}$ of 0.79, nearly twice that of bare Zn, demonstrating that the pre-embedded Zn^{2+} effectively suppresses dense CD stacking, preserves continuous inter-particle transport channels, and exposes more zincophilic sites for selective Zn^{2+} conduction.[38] As CMC-Na itself contains abundant hydroxyl and carboxylate groups and is able to coordinate Zn^{2+}, its possible contribution to the interfacial kinetics deserves explicit consideration. The CD@Zn electrode serves as a direct internal control in this respect, since it contains the same amount of CMC-Na (10%, mass fraction) as zCD@Zn, the identity of the active phase being the only difference. Were the binder to dominate the interfacial behaviour, CD@Zn should display kinetics similar to those of zCD@Zn; in reality, CD@Zn exhibits a higher E_a (30.83 kJ/mol) and a lower $tz_{n^{2+}}$ (0.39) than even the bare Zn electrode, which excludes a binder-dominated mechanism. Moreover, CMC-Na constitutes only 10% (mass fraction) of the coating and primarily serves as a binder, rather than as the dominant functional component of the protective layer. In contrast, zCDs account for 90% (mass fraction) of the coating, constituting the predominant functional phase at the Zn/electrolyte interface. Therefore, the facilitated Zn^{2+} desolvation and selective Zn^{2+} transport observed in this system can be predominantly attributed to the intrinsic interfacial properties of zCDs, rather than to the contribution of the CMC-Na binder. Consistent with the desolvation and

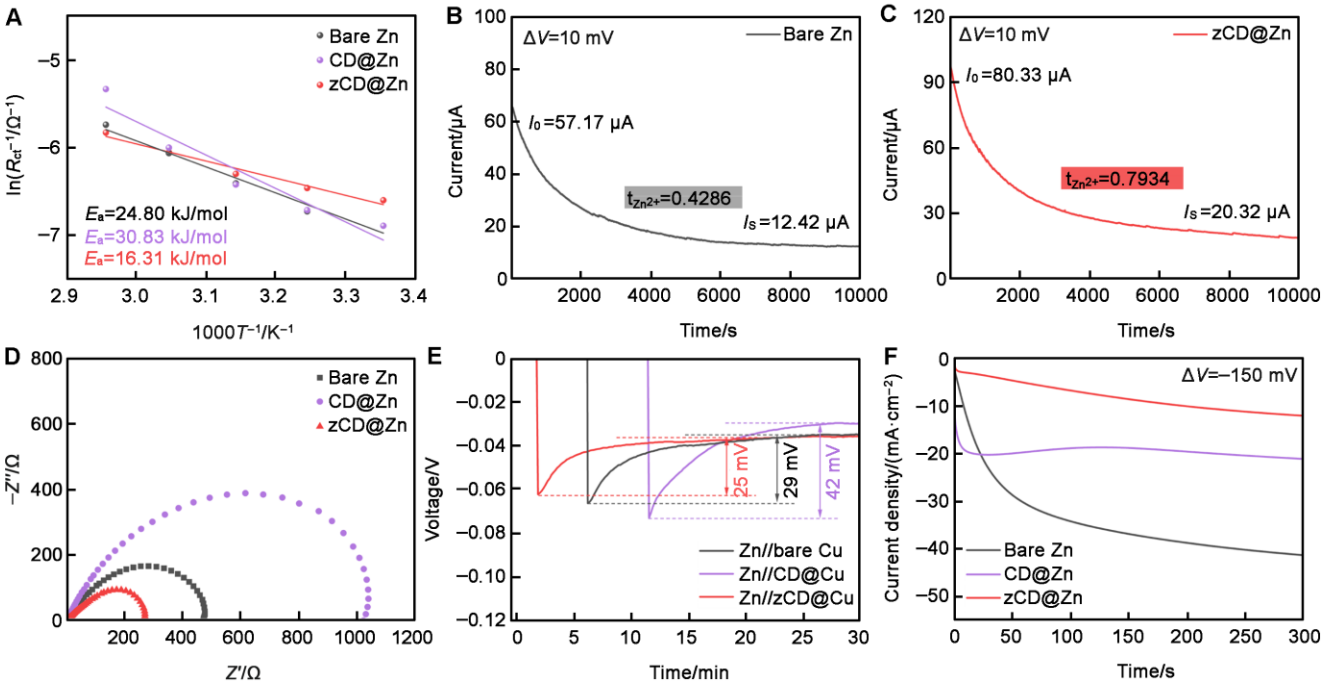


Fig. 3 Zn^{2+} transport and deposition kinetics of bare Zn, CD@Zn, and zCD@Zn

(A) Desolvation energies of bare Zn, CD@Zn, and zCD@Zn; (B, C) Zn^{2+} transference numbers (t_{Zn2+}) of bare Zn (B) and zCD@Zn (C); (D) EIS curves of bare Zn, CD@Zn, and zCD@Zn symmetric cells after 10 cycles at 1 mA/cm^2 and 1 mA·h·cm^{-2}; (E) nucleation overpotentials of bare Cu, CD@Cu, and zCD@Cu; (F) chronoamperometry curves of bare Zn, CD@Zn, and zCD@Zn.

https://doi.org/10.1007/s40242-026-6206-x

transport results, EIS measurements (Fig. 3D) reveal that the charge transfer resistance (R_{ct}) follows the order CD@Zn>bare Zn>zCD@Zn. The nucleation overpotentials, measured in Zn||Cu asymmetric cells (Fig. 3E), further corroborate this trend: zCD@Cu displays the lowest overpotential of 25 mV, compared with 29 mV for bare Cu and 42 mV for CD@Cu. This finding is independently corroborated by cyclic voltammetry (CV) measurements on Zn||Cu half cells (Fig. S10 in the SI), which reveal the smallest nucleation overpotential for zCD@Zn. Together, these results demonstrate that the zCD coating effectively reduces the nucleation energy barrier, thereby promoting spatially uniform Zn deposition and suppressing dendrite initiation.

Chronoamperometry at −150 mV (Fig. 3F) reveals distinct Zn^{2+} diffusion behaviors among the three electrodes. The bare Zn electrode shows a continuously increasing current, characteristic of uncontrolled 2D diffusion that drives dendrite propagation.[39] CD@Zn exhibits persistent current fluctuation, reflecting unstable Zn^{2+} transport through the aggregated coating layer. In contrast, zCD@Zn rapidly reaches a stable current plateau, demonstrating a well-regulated 3D diffusion process that favors uniform and compact Zn deposition.

The advantageous interfacial kinetics endowed by the zCD coating translate directly into superior electrochemical performance. Galvanostatic Zn plating/stripping was first examined in symmetric cells at 1 mA/cm² with an areal capacity of 1 mA·h·cm⁻² (Fig. 4A). The bare Zn cell fails within 200 h, accompanied by erratic voltage fluctuations characteristic of dendrite-induced short-circuiting. The CD@Zn cell extends the lifespan to nearly 700 h; notably, its failure is signalled by an abrupt surge in polarization voltage rather than a short circuit, which can be ascribed to the progressive blockage of the ion transport pathways within the densely stacked CD layer by the deposited Zn, consistent with the retarded Zn^{2+} transport kinetics revealed in Fig. 3. In stark contrast, the zCD@Zn cell operates stably for over

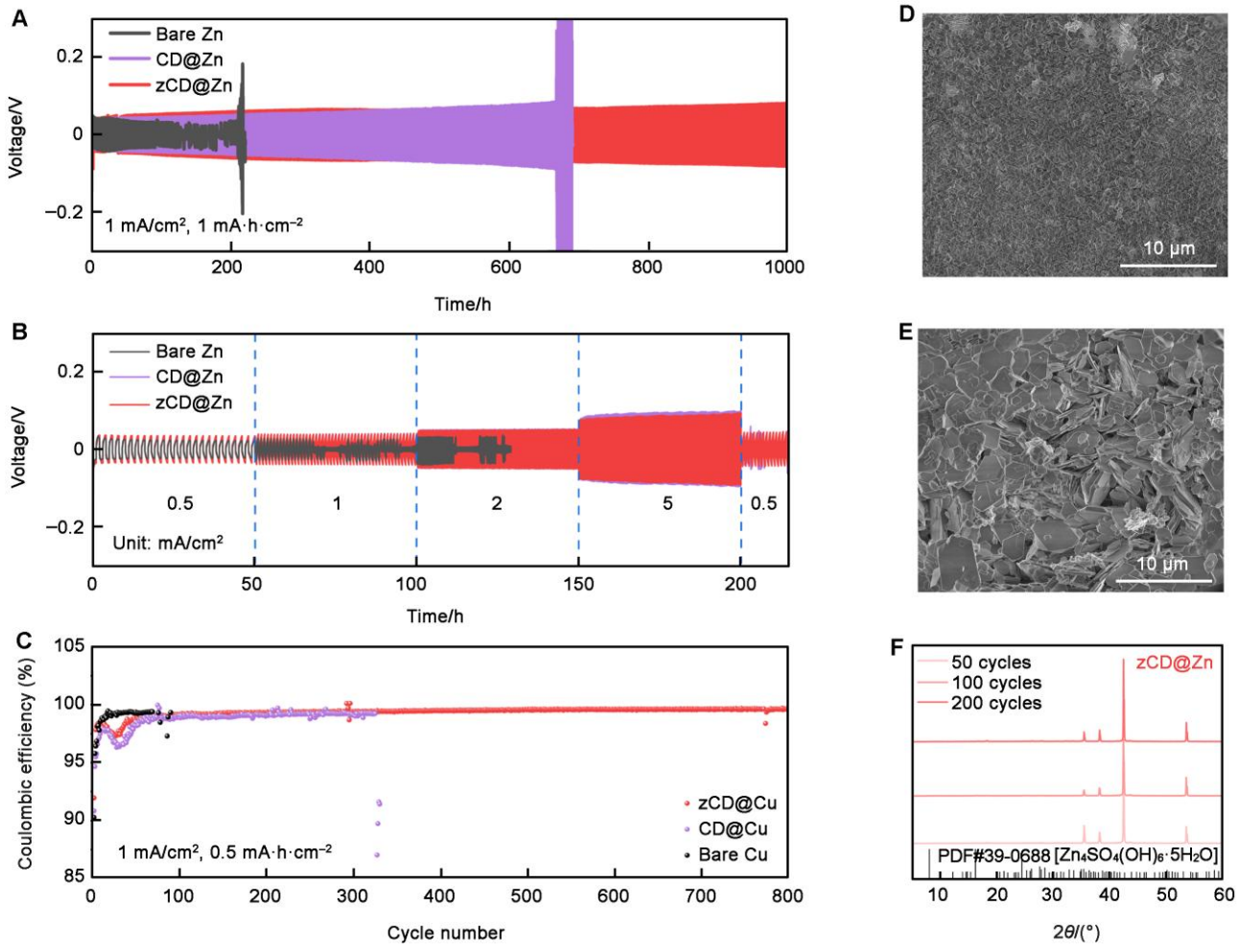


Fig. 4 Long-term cycling stability and reversibility of bare Zn, CD@Zn, and zCD@Zn

(A) Galvanostatic cycling performance of bare Zn, CD@Zn, and zCD@Zn symmetric cells at 1 mA/cm² and 1 mA·h·cm⁻²; (B) rate performance of the symmetric cells at stepwise current densities from 0.5 mA/cm² to 5 mA/cm² with a fixed capacity of 0.5 mA·h·cm⁻²; (C) Coulombic efficiencies of Zn||Cu half cells with bare Cu, CD@Cu, and zCD@Cu electrodes at 1 mA/cm² and 0.5 mA·h·cm⁻²; (D, E) SEM images of zCD@Zn (D) and bare Zn (E) after 200 cycles; (F) XRD patterns of zCD@Zn after 50, 100, and 200 cycles.

https://doi.org/10.1007/s40242-026-6206-x

1000 h with a small and nearly constant voltage hysteresis, demonstrating the durability of the zCD-protected interface. The rate capability was further evaluated at stepwise current densities from 0.5 mA/cm² to 5 mA/cm² (Fig. 4B). The bare Zn cell fails when the current density is raised to 5 mA/cm², while the CD@Zn cell survives but exhibits markedly enlarged polarization. In contrast, the zCD@Zn cell maintains stable and reversible plating/stripping across all tested current densities; more importantly, its voltage profile immediately recovers and remains stable when the current density is returned to 0.5 mA/cm², indicating that the facilitated desolvation and rapid Zn^{2+} transport through the zCD layer (Fig. 3, A and D) enable fast and reversible Zn deposition even under high-rate operation.

The reversibility of Zn deposition was quantified by Coulombic efficiency (CE) measurements in Zn||Cu half cells at 1 mA/cm² and 0.5 mA·h·cm^{-2} (Fig. 4C and Fig. S11 in the SI). The cell with bare Cu fails within 70 cycles, whereas the CD@Cu-based cell sustains 325 cycles before the CE decays. Remarkably, the zCD@Cu-based cell operates stably for over 800 cycles with an average CE of 99.5%, confirming the highly reversible Zn plating/stripping enabled by the zCD coating.

Post-mortem analyses of the cycled electrodes provide direct evidence for the stabilized interface. After 200 cycles, the zCD@Zn electrode presents a uniform and compact Zn deposition layer (Fig. 4D), whereas the bare Zn surface is covered by fragmented and disordered Zn deposits with inhomogeneously sized nuclei (Fig. 4E). XRD patterns collected after 50, 100, and 200 cycles further reveal the effective suppression of parasitic reactions: characteristic diffraction peaks of ZHS by-products emerge on bare Zn after only 50 cycles and intensify with prolonged cycling (Fig. S12 in the SI), whereas they remain nearly absent on zCD@Zn throughout 200 cycles (Fig. 4F).[40] These results collectively demonstrate that the zCD coating simultaneously homogenizes Zn deposition and suppresses interfacial side reactions, which accounts for its exceptional cycling stability and reversibility.

To evaluate the practical viability of the zCD-protected anode, full cells were assembled by pairing bare Zn or zCD@Zn anodes with α-MnO_2 cathodes. The phase purity of the α-MnO_2 cathode was confirmed by XRD (Fig. S13 in the SI). Cyclic voltammetry (CV) was first performed at 0.2 mV/s (Fig. 5A). Both cells exhibit two pairs of redox peaks characteristic of the MnO_2 cathode, associated with the H^+ and Zn^{2+} (de)intercalation processes, and the nearly identical peak positions confirm that the zCD coating does not alter the intrinsic redox chemistry of the full cell. Nevertheless, the zCD@Zn-based cell delivers a noticeably larger enclosed CV area and a narrower separation between the redox peaks, indicating enhanced capacity utilization and reduced electrochemical polarization. Consistently, electrochemical impedance spectroscopy (Fig. S14 in the SI) reveals a lower charge-transfer resistance for the zCD@Zn full cell than for its bare Zn counterpart, corroborating the accelerated

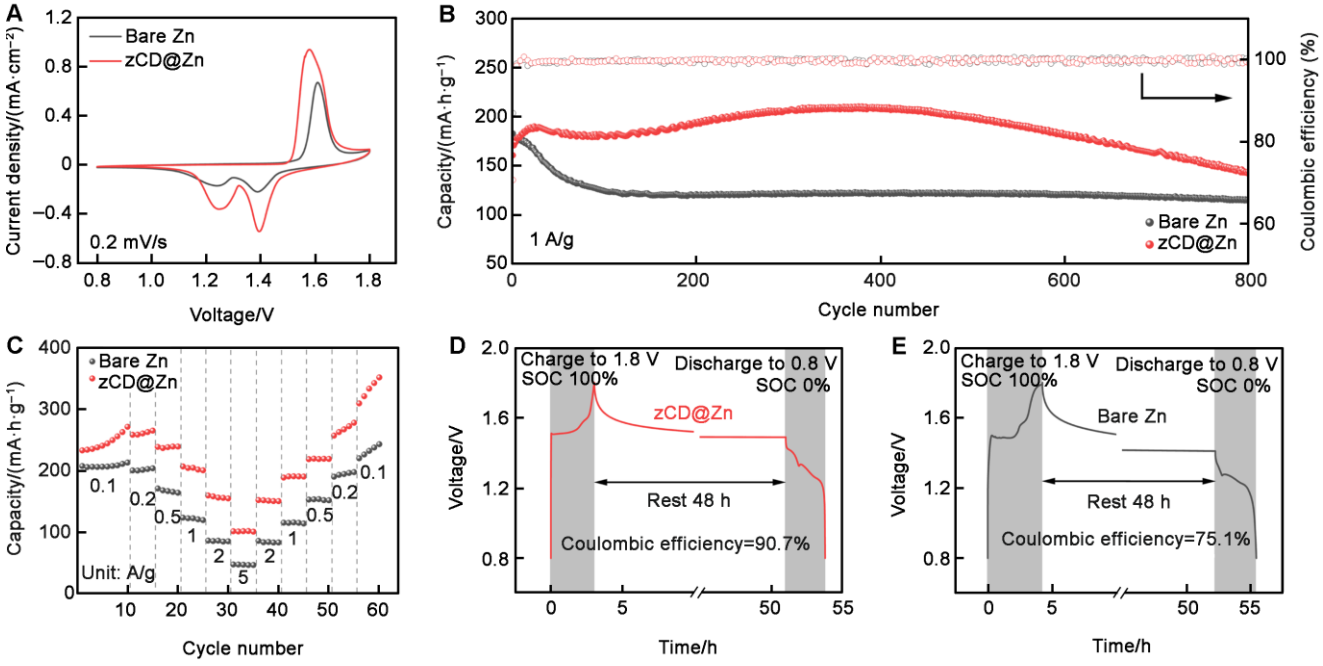


Fig. 5 Electrochemical performance of Zn||MnO_2 full cells

(A) CV curves of Zn||MnO_2 full cells with bare Zn and zCD@Zn anodes at a scan rate of 0.2 mV/s; (B) long-term cycling performance of the full cells at 1 A/g; (C) rate performance of the full cells at current densities from 0.1 A/g to 5 A/g; (D, E) voltage profiles of the self-discharge tests for the full cells with zCD@Zn (D) and bare Zn (E) anodes: charged to 1.8 V, rested for 48 h, and then discharged to 0.8 V (SOC: state of charge).

https://doi.org/10.1007/s40242-026-6206-x

interfacial kinetics endowed by the zCD coating.

The long-term cycling stability of the full cells was examined at 1 A/g (Fig. 5B). After 800 cycles, the zCD@Zn-based cell retains a reversible capacity of 141.26 mA·h·g^{-1}, markedly surpassing the 114.74 mA·h·g^{-1} delivered by the bare Zn cell. The bare Zn cell suffers a rapid capacity decay within the initial cycles, whereas the zCD@Zn cell undergoes a gradual activation process followed by substantially slower fading. This divergence originates from the interfacial stability of the anode. For the unprotected anode, persistent corrosion and hydrogen evolution continuously consume active Zn and electrolyte water, while the concomitant accumulation of OH^- disturbs the electrolyte pH, which in turn promotes the precipitation of insulating zinc hydroxide sulfate on the cathode surface and aggravates Mn dissolution, jointly accelerating capacity decay.[41] Meanwhile, the passivating by-products raise the interfacial resistance of the anode, so that the cell reaches the cut-off voltage prematurely and the accessible capacity shrinks. By suppressing these parasitic processes at the source, the zCD coating preserves a stable electrochemical environment for both electrodes, thereby enabling the superior capacity retention of the full cell. The rate capability further highlights the kinetic advantage of the zCD-protected anode (Fig. 5C). As the current density is increased stepwise from 0.1 A/g to 5 A/g, the zCD@Zn-based cell consistently delivers higher capacities than the bare Zn cell; particularly, at 5 A/g it still affords 101.21 mA·h·g^{-1}, whereas the bare Zn cell fades to merely 47.11 mA·h·g^{-1}.

To further evaluate the influence of the protected Zn anode on the MnO_2 cathode stability, the dissolved Mn species in the electrolyte after cycling were quantified by inductively coupled plasma optical emission spectrometry (ICP-OES, Fig. S15 in the SI). After 100 cycles, the Mn concentration in the electrolyte of the zCD@Zn||MnO_2 cell was 12.56 mg/L, which is lower than that of the bare Zn||MnO_2 cell (19.89 mg/L), indicating suppressed Mn dissolution. In addition, the lighter coloration of the cathode-side case after cycling for the zCD@Zn cell compared with the bare Zn cell further suggests reduced migration/deposition of Mn-containing species (Fig. S16 in the SI). These results demonstrate that stabilization of the Zn/electrolyte interface by the zCD coating not only improves Zn reversibility but also mitigates MnO_2 cathode degradation during cycling.

Finally, the self-discharge behavior was assessed by charging the full cells to 1.8 V, resting them for 48 h, and then discharging to 0.8 V (Fig. 5, D and E). The zCD@Zn-based cell retains 90.7% of its pre-rest capacity, considerably higher than the 75.1% of the bare Zn cell. Although the excess Zn reservoir of the full cell masks the direct loss of anode active material, the corrosion-induced OH^- accumulation perturbs the electrolyte pH and, through the same cathode-anode coupling as under cycling, promotes the precipitation of insulating ZHS on the cathode and aggravates Mn dissolution, thereby eroding the cathode capacity. To further clarify the origin of self-discharge, EIS measurements before and after 48 h of static rest were conducted (Fig. S17 in the SI). After resting, the bare Zn||MnO_2 cell exhibited a much larger increase in R_{ct} compared with the zCD@Zn||MnO_2 cell, indicating more severe interfacial degradation caused by Zn corrosion and parasitic reactions. The markedly reduced capacity loss of the zCD@Zn cell thus confirms that the protective coating remains effective under shelf-rest conditions, underscoring its significance for the calendar life of practical zinc-ion batteries.

3 Conclusions

In summary, we have developed zinc pre-embedded carbon dots as a dual-functional protective layer for Zn metal anodes, in which the zinc pre-embedding strategy effectively resolves the aggregation dilemma intrinsic to nanoscale CDs. The pre-embedded Zn^{2+} occupies the coordination sites of the surface functional groups and introduces steric hindrance between adjacent CDs, thereby suppressing dense stacking, preserving continuous inter-particle ion-transport channels, and rendering the zincophilic carbonyl, hydroxyl, and amino groups fully accessible. Coupled with its hydrophobic character, the zCD layer simultaneously suppresses water-induced corrosion and hydrogen evolution, facilitates Zn^{2+} desolvation (E_a reduced to 16.31 kJ/mol), raises the t_{Zn2+} to 0.79, lowers the nucleation overpotential to 25 mV, and regulates three-dimensional Zn^{2+} diffusion, which together enable uniform and dendrite-free Zn deposition. Consequently, the zCD@Zn anode delivers a cycling lifespan of over 1000 h in symmetric cells and an average Coulombic efficiency of 99.5% over 800 cycles in half cells, while the full cell with an MnO_2 cathode retains 141.26 mA·h·g^{-1} after 800 cycles at 1 A/g (87.9% capacity retention), delivers 101.21 mA·h·g^{-1} at 5 A/g, and maintains 90.7% of its capacity after a 48 h rest. More broadly, the pre-embedding concept — employing pre-coordinated metal ions as inter-particle spacers to expose functional sites — provides a general design principle for nanomaterial-based interfacial engineering and can be potentially extended to other metal anode chemistries toward practical aqueous batteries.

From a manufacturing perspective, several features of this strategy are favorable for practical implementation. The protective layer is fabricated by blade coating using an aqueous slurry, a process that is compatible with established electrode-manufacturing procedures while eliminating the need for organic solvents. In addition, the precursors,

https://doi.org/10.1007/s40242-026-6206-x

including pyromellitic dianhydride, *o*-phenylenediamine, and zinc acetate, are inexpensive and commercially available, while CMC-Na is a widely used binder in battery manufacturing. Nevertheless, further efforts are required to achieve highly uniform coatings over large-area, thin Zn foils and to validate their long-term reliability under practically relevant conditions, including high areal loading, lean electrolyte, and extended calendar aging. These considerations represent important directions for the further development and practical implementation of this interfacial protection strategy.

Supporting Information

The detailed experimental procedures and the supplementary materials are available in the online version of this article at http://dx.doi.org/10.1007/s40242-026-6206-x.

Acknowledgements

This work was supported by the National Natural Science Foundation of China (Nos. U24A20565, 22575057) and the Science and Technology Commission of Shanghai Municipality, China (No. 25ZR1401024).

Conflicts of Interest

The authors declare no conflicts of interest.

References

[1] Zhang N., Chen X., Yu M., Niu Z., Cheng F., Chen J., *Chemical Society Reviews*, **2020**, *49*, 4203.
[2] Blanc L. E., Kundu D., Nazar L. F., *Joule*, **2020**, *4*, 771.
[3] Li C., Jin S., Archer L. A., Nazar L. F., *Joule*, **2022**, *6*, 1733.
[4] Xie X., Liang S., Gao J., Guo S., Guo J., Wang C., Xu G., Wu X., Chen G., Zhou J., *Energy & Environmental Science*, **2020**, *13*, 503.
[5] Tang M., Liu Q., Zou X., Zhang B., An L., *Advanced Materials*, **2025**, *37*, 2501361.
[6] Yuan L., Hao J., Kao C., Wu C., Liu H., Dou S., Qiao S., *Energy & Environmental Science*, **2021**, *14*, 5669.
[7] Ma H., Chen H., Chen M., Li A., Han X., Ma D., Zhang P., Chen J., *Nature Communications*, **2025**, *16*, 1014.
[8] Zhu K., Xie W., Yang W., *Angewandte Chemie International Edition*, **2025**, *64*, e202516233.
[9] Khamsanga S., Uyama H., Nuanwat W., Pattananuwat P., *Scientific Reports*, **2022**, *12*, 8689.
[10] Huang R., Huang X., Wu T., Liu Y., Wang M., Wang W., Zhang H., Ma S., Li J., Wu D., Tian J., Tian Z., *Journal of the American Chemical Society*, **2026**, *148*, 30815.
[11] Kim H. J., Kim S., Kim S., Kim S., Heo K., Lim J., Yashiro H., Shin H., Jung H., Lee Y. M., Myung S., *Advanced Materials*, **2024**, *36*, 2308592.
[12] Ren Q., Tang X., He K., Zhang C., Wang W., Guo Y., Zhu Z., Xiao X., Wang S., Lu J., Yuan Y., *Advanced Functional Materials*, **2024**, *34*, 2312220.
[13] Wu L., Yuan H., An Y., Sun J., Liu Y., Tang H., Yang W., Cui L., Li J., An Q., Zhang Y., Xu L., Mai L., *Angewandte Chemie International Edition*, **2025**, *64*, e202419495.
[14] Yang H., Zhu K., Xie W., Zhang L., Jiang W., Li W., Wang Z., Yang W., *Energy & Environmental Science*, **2023**, *16*, 4549.
[15] Li T., Li X., Yang H., Zhou Y., Li X., Su M., Dou A., Zhang P., Wu X., Naveed A., Sumner J., Liu Y., *Materials Today Energy*, **2024**, *40*, 101513.
[16] Tang Q., Zhang X., Zhou S., Xu Y., He L., Chen S., Cai W., Wei Z., *Energy & Environmental Science*, **2025**, *18*, 9538.
[17] Liu X., Wang X., Yao J., Li J., Gan Y., Wu Z., Zheng J., Hao W., Lv L., Tao L., Zhang J., Wang H., Ji X., Wan H., Wang H., *Advanced Energy Materials*, **2024**, *14*, 2400090.
[18] Deng Q., You S., Min W., Xu Y., Lin W., Lu J., Yang C., *Advanced Materials*, **2024**, *36*, 2312924.
[19] Zeng Y., Pei Z., Guo Y., Luan D., Gu X., Lou X. W., *Angewandte Chemie International Edition*, **2023**, *62*, e202312145.
[20] Wang Y., Jiang X., Liang W., Tawiah B., Wang Y., Jia H., Wong W.-Y., *Advanced Materials*, **2025**, *37*, 2503086.
[21] Chen Z., Liu Y., Kang Z., *Accounts of Chemical Research*, **2022**, *55*, 3110.
[22] Zhang Z., Zhou X., Dong J., Xue T., Di Y., Li B., Zhao N., Dai L., Wang L., He Z., *Advanced Energy Materials*, **2024**, *14*, 2402721.
[23] Zhang H., Li S., Xu L., Momen R., Deng W., Hu J., Zou G., Hou H., Ji X., *Advanced Energy Materials*, **2022**, *12*, 2200665.
[24] Yang H., Zhu K., Xie W., Yang W., *ACS Nano*, **2025**, *19*, 1433.
[25] Song T., Ma Q., Zhang X., Ni J., He T., Xiong H., *Chemical Engineering Journal*, **2023**, *471*, 144735.
[26] Boukhvalov D. W., Osipov V. Y., Murzalinov D., Serikkanov A., Bi H., *Carbon*, **2024**, *225*, 119101.
[27] Emam A. N., Loutfy S. A., Mostafa A. A., Awad H., Mohamed M. B., *RSC Advances*, **2017**, *7*, 23502.
[28] Wu Z., Wang B., Ni J., Sun Z., Zhang X., Xiong H., *Nano Letters*, **2024**, *24*, 9675.
[29] Wang B., Jia X., Sun H., Wu Z., Luo X., Mao Y., Xiong H., *Chemical Engineering Journal*, **2025**, *526*, 170852.
[30] Hu F., Fu Q., Li Y., Yan C., Xiao D., Ju P., Hu Z., Li H., Ai S., *Food Chemistry*, **2024**, *431*, 137097.
[31] Song T., Ma Q., Wang B., Zhang X., Wang Y., Xiong H., *Angewandte Chemie International Edition*, **2025**, *64*, e202503655.
[32] Zhu Y., Liang G., Cui X., Liu X., Zhong H., Zhi C., Yang Y., *Energy & Environmental Science*, **2024**, *17*, 369.
[33] Ren B., Hu S., Chen A., Zhang X., Wei H., Jiang J., Chen G., Zhi C., Li H., Liu Z., *Advanced Energy Materials*, **2024**, *14*, 2302970.
[34] Yang F., Yuwono J. A., Hao J., Long J., Yuan L., Wang Y., Liu S., Fan Y., Zhao S., Davey K., Guo Z., *Advanced Materials*, **2022**, *34*, 2206754.
[35] Xu D., Ren X., Xu Y., Wang Y., Zhang S., Chen B., Chang Z., Pan A., Zhou H., *Advanced Science*, **2023**, *10*, 2303773.
[36] Yuan G., Qiu Z., Su Y., Hu J., Li W., Liu Z., Shakouri M., Pang H., *Advanced Materials*, **2026**, *38*, e21287.
[37] Hong L., Guan J., Tan Y., Chen Y., Liu Y.-S., Huang W., Yu C., Zhou Y., Chen J., Wang K., *Energy & Environmental Science*, **2024**, *17*, 3157.
[38] Cai X., Tian W., Zhang Z., Sun Y., Yang L., Mu H., Lian C., Qiu H., *Advanced Materials*, **2024**, *36*, 2307727.
[39] Li G., Zhao Z., Zhang S., Sun L., Li M., Yuwono J. A., Mao J., Hao J., Vongsvivut J., Xing L., Zhao C., Guo Z., *Nature Communications*, **2023**, *14*, 6526.
[40] Tian S., Hwang T., Zhang Z., Wu S., Mashhadian A., Zhang R., Milazzo T., Luo T., Jian R., Li T., Cho K., Xiong G., *ACS Nano*, **2025**, *19*, 3135.
[41] Han Y., Wang F., Yan L., Luo L., Qin Y., Zhu C., Hao J., Chen Q., Zou X., Zhou Y., Xiang B., *Chemical Science*, **2024**, *15*, 12336.